

## Sunlight transmission through desert dust and marine aerosols: Diffuse light corrections to Sun photometry and pyrradiometry

P. B. Russell,<sup>1</sup> J. M. Livingston,<sup>2</sup> O. Dubovik,<sup>3</sup> S. A. Ramirez,<sup>4</sup> J. Wang,<sup>5</sup> J. Redemann,<sup>4</sup> B. Schmid,<sup>4</sup> M. Box,<sup>6</sup> and B. N. Holben<sup>7</sup>

Received 27 October 2003; revised 30 January 2004; accepted 26 February 2004; published 27 April 2004.

[1] Desert dust and marine aerosols are receiving increased scientific attention because of their prevalence on intercontinental scales and their potentially large effects on Earth radiation, climate, other aerosols, clouds, and precipitation. The relatively large size of dust and marine aerosol particles produces scattering phase functions that are strongly forward peaked. Hence Sun photometry and pyrradiometry of these aerosols are more subject to diffuse light errors than is the case for smaller aerosols. We quantify these diffuse light effects for common Sun photometer and pyrradiometer fields of view (FOV), using data on dust and marine aerosols from (1) Aerosol Robotic Network (AERONET) measurements of sky radiance and solar beam transmission and (2) in situ measurements of aerosol layer size distribution and chemical composition. Accounting for particle nonsphericity is important when deriving dust size distribution from both AERONET and in situ aerodynamic measurements. We obtain correction factors that can be applied to Sun photometer or pyrradiometer results for aerosol optical depth (AOD) or direct beam transmission. The corrections are negligible (less than  $\sim 1\%$  of AOD) for Sun photometers with narrow FOV (half-angle  $\eta < \sim 1^\circ$ ), but they can be as large as 10% of AOD at 354 nm wavelength for Sun photometers with  $\eta = 1.85^\circ$ . For pyrradiometers (which can have  $\eta$  up to  $\sim 2.8^\circ$ ), corrections can be as large as 16% at 354 nm. AOD correction factors are well correlated with AOD wavelength dependence (hence Ångström exponent). We provide best fit equations for determining correction factors from Ångström exponents of uncorrected AOD spectra, and we demonstrate their application to vertical profiles of multiwavelength AOD.

**INDEX TERMS:** 0305 Atmospheric Composition and Structure: Aerosols and particles (0345, 4801); 0345 Atmospheric Composition and Structure: Pollution—urban and regional (0305); 0360 Atmospheric Composition and Structure: Transmission and scattering of radiation; 0365

Atmospheric Composition and Structure: Troposphere—composition and chemistry; 0394 Atmospheric Composition and Structure: Instruments and techniques; **KEYWORDS:** Sun photometer, aerosol, diffuse

**Citation:** Russell, P. B., J. M. Livingston, O. Dubovik, S. A. Ramirez, J. Wang, J. Redemann, B. Schmid, M. Box, and B. N. Holben (2004), Sunlight transmission through desert dust and marine aerosols: Diffuse light corrections to Sun photometry and pyrradiometry, *J. Geophys. Res.*, 109, D08207, doi:10.1029/2003JD004292.

### 1. Introduction

[2] Recent studies have focused renewed attention on the properties and effects of desert dust and marine aerosols. Plumes of desert dust extending downwind from continents are a prominent feature of satellite imagery [Chiapello *et al.*, 1999; Moulin *et al.*, 2001; Prospero *et al.*, 2002]. Satellite

data analyses also reveal the important role of marine sea-salt aerosols [Haywood *et al.*, 1999]. Both desert dust and marine aerosols can have significant effects on Earth radiation balance and climate [Sokolik and Toon, 1996; Tegen *et al.*, 1996; Haywood *et al.*, 2001a, 2001b; Jacobson, 2001], and they can modify the properties and effects of other aerosols, clouds and precipitation [Jones and Slingo, 1996; O'Dowd *et al.*, 1999; Li-Jones and Prospero, 1998; Rosenfeld, 2000; Rosenfeld *et al.*, 2002]. Consequently, measurements of desert dust and marine aerosol properties and radiative effects from surface, air, and space have been emphasized in several recent experiments, including ACE-2 [Raes *et al.*, 2000; Russell and Heintzenberg, 2000], SHADE [Haywood *et al.*, 2001a, 2001b, 2003], PRIDE [Reid *et al.*, 2003], and ACE-Asia [Huebert *et al.*, 2003]. Among the fundamental properties targeted in these campaigns is the wavelength-dependent aerosol optical depth, derived from Sun-photometer-measured solar beam transmissions and satellite-measured reflectances. Important

<sup>1</sup>NASA Ames Research Center, Moffett Field, California, USA.

<sup>2</sup>SRI International, Menlo Park, California, USA.

<sup>3</sup>Goddard Earth Sciences and Technology Center, NASA Goddard Space Flight Center, Greenbelt, Maryland, USA.

<sup>4</sup>Bay Area Environmental Research Institute, Sonoma, California, USA.

<sup>5</sup>Brookhaven National Laboratory, Upton, New York, USA.

<sup>6</sup>School of Physics, University of New South Wales, Sydney, New South Wales, Australia.

<sup>7</sup>Laboratory for Atmospheres, NASA Goddard Space Flight Center, Greenbelt, Maryland, USA.

**Table 1.** Diffuse Light Correction Factors Derived by Previous Studies

Method	FOV Half-Angle $\eta$ , deg	Wavelength, $\mu\text{m}$	Particle Model <sup>a</sup>	Correction Factor $C \equiv \tau/\tau'$	Reference
<b>Aerosols</b>					
Monte Carlo and analytical fit	1.0, 1.2, 2.5		aerosol, $R_{\text{eff}} = 0.2 \mu\text{m}$	$\leq 1.01$	<i>Kinne et al.</i> [1997]
Monte Carlo and analytical fit	1.0, 1.2, 2.5		haze-L, $R_{\text{eff}} = 0.5 \mu\text{m}$	$\leq 1.02$	<i>Kinne et al.</i> [1997]
Monte Carlo and analytical fit	1.2	0.55	aerosol, $n(r) = r^{-\nu}$ , $\nu = 4, 3.5$ ( $R_{\text{eff}} = 0.07, 0.39 \mu\text{m}$ )	1.009, 1.03	<i>Shiobara and Asano</i> [1994]
<i>Reagan et al.</i> [1992] and <i>Box and Deepak</i> [1979]	$\leq 2.2$	$\geq 0.38$	post-Pinatubo volcanic aerosol, $R_{\text{eff}} = 0.2\text{--}0.6 \mu\text{m}$	$\leq 1.02$	<i>Russell et al.</i> [1993b]
<i>Reagan et al.</i> [1992] and <i>Box and Deepak</i> [1979]	$\leq 2.2$	$\geq 0.38$	post-Pinatubo volcanic aerosol, $R_{\text{eff}} = 0.9 \mu\text{m}$	$\leq 1.05$	<i>Russell et al.</i> [1993b]
Analytical with approximations	$\leq 8$	any	various aerosols, $n(r) = r^{-\nu}$ , $\nu = 5$ to 2 ( $R_{\text{eff}} = 0.02$ to $7.5 \mu\text{m}$ )	1.0–1.8	<i>Box and Deepak</i> [1979]
Analytical with approximations	$\leq 8$	0.55	various aerosols, modified gamma	1.0–2.0	<i>Box and Deepak</i> [1979]
<b>Clouds</b>					
Monte Carlo and analytical fit	1.0, 1.2, 2.5		various clouds, $R_{\text{eff}} = 6\text{--}177 \mu\text{m}$	1.2–2.5	<i>Kinne et al.</i> [1997]
Monte Carlo and analytical fit	1.2	0.55	cirrostratus clouds	2.0	<i>Shiobara and Asano</i> [1994]

<sup>a</sup> $R_{\text{eff}}$  is the effective (area-weighted) radius.

effects include not only those on total (diffuse plus direct) solar fluxes, but also on the energy in the direct solar beam, as measured by pyrhemometers and cavity radiometers [Halthore et al., 1997].

[3] As noted by many studies [e.g., Grassl, 1971; Box and Deepak, 1979; Russell et al., 1993a, 1993b; Shiobara and Asano, 1994; Kinne et al., 1997; Eck et al., 1999], Sun photometers and pyrhemometers have nonzero fields of view that accept some diffuse light in addition to the direct solar beam. As a result, uncorrected Sun photometer measurements can overestimate direct beam transmission  $T$  and underestimate optical depth  $\tau$ .

[4] The previous studies mentioned above have quantified the diffuse light effect for several types of aerosols and clouds and for different Sun photometer fields of view (FOV). In general, the effect increases with particle size and instrument FOV. Representative results from previous studies are shown in Table 1. As an example, Kinne et al. [1997] give results for two aerosol models with effective (area-weighted) radii  $R_{\text{eff}} = 0.2$  and  $0.5 \mu\text{m}$ , several cloud models with  $R_{\text{eff}} = 6\text{--}177 \mu\text{m}$ , and FOV half angles  $\eta = 1^\circ$ ,  $1.2^\circ$ , and  $2.5^\circ$ . They found that the correction factor  $C$ , defined as

$$C \equiv \tau/\tau', \quad (1)$$

where  $\tau$  and  $\tau'$  are true and apparent optical depths, was 1.02 or less for their aerosol models and FOV half angle up to  $2.5^\circ$ , but that it could be as large as 2.47 for their cloud models. Similarly, Shiobara and Asano [1994] found correction factors  $C$  of only 1.009 and 1.03 for their two aerosol models (which had  $R_{\text{eff}} = 0.07$  and  $0.39 \mu\text{m}$ , respectively), but 1.96 for their cirrus cloud phase function (all results for wavelength  $\lambda = 0.5 \mu\text{m}$ ,  $\eta = 1.2^\circ$ ). Russell et al. [1993b] found that post-Pinatubo stratospheric aerosol size distributions with  $R_{\text{eff}} = 0.2\text{--}0.6 \mu\text{m}$  had correction factors  $C < 1.02$  for  $\lambda = 0.38$  to  $1.02 \mu\text{m}$  and  $\eta$  up to  $2.2^\circ$ . However, a size distribution with  $R_{\text{eff}} = 0.9 \mu\text{m}$  had  $C = 1.05$  at  $\lambda = 0.38 \mu\text{m}$  and  $\eta = 2.2^\circ$ .

[5] Box and Deepak [1979] give correction factors for a wide range of power law and unimodal modified gamma distributions. However, their results are not given as a

function of  $R_{\text{eff}}$ . Also, it is now recognized that many aerosol size distributions have two or more size modes and are often not well represented by power law or unimodal distributions. Hence it is difficult to translate the above results to the aerosol conditions of specific Sun photometer measurements: especially conditions of desert dust and marine haze, where particle sizes can significantly exceed the aerosol sizes in, e.g., the studies of Kinne et al. [1997] and Shiobara and Asano [1994]. The nonspherical shape of desert dust particles also raises questions about the applicability of the above aerosol results, which assumed spherical aerosol particles [cf. Dubovik et al., 2002a, 2002b; Kalashnikova and Sokolik, 2002].

## 2. Data Sources

[6] Recent measurements by the Aerosol Robotic Network (AERONET) of Sun/sky radiometers [Holben et al., 1998] have produced a large body of data on desert dust and maritime aerosols, including optical depth spectra, scattering phase functions, size distributions, complex refractive indices, and single-scattering albedos. These parameters are retrieved from combined measurements of scattered light (skylight) and direct beam transmission using the algorithm of Dubovik and King [2000]. The results [e.g., Tanré et al., 2001; Dubovik et al., 2002a; Levy et al., 2003; Smirnov et al., 2002] show that desert dust and maritime aerosols typically have bimodal size distributions with coarse-mode  $R_{\text{eff}} = 1.1\text{--}3.2 \mu\text{m}$ . These coarse-mode aerosols thus fall in a gap between the aerosol and cloud models cited above (aerosol  $R_{\text{eff}} = 0.2\text{--}0.9 \mu\text{m}$ ; cloud  $R_{\text{eff}} = 6\text{--}177 \mu\text{m}$ ). Because they are based on, and consistent with, measurements of the angular distribution of diffuse skylight, these AERONET results provide a very useful basis for deriving diffuse light correction factors.

[7] We will also supplement the AERONET results with size distributions and compositions measured by airborne instrumentation specially designed to admit large particles at aircraft speeds [Wang et al., 2002]. These in situ results have been shown to produce aerosol layer optical depth spectra that agree with layer optical depth spectra measured

by tracking Sun photometer on the same aircraft [Wang *et al.*, 2002; Schmid *et al.*, 2003].

### 3. Calculation Methods

#### 3.1. Analytical Formulation

[8] To calculate diffuse light correction factors, we follow the analytical formulation of *Shiobara and Asano* [1994] and *Kinne et al.* [1997]. Both these studies performed Monte Carlo calculations of all orders of light scattered into the Sun photometer FOV. They showed that their Monte Carlo results, over a range of slant-path optical depths from 0 to 6, were well approximated by the analytical result

$$C \equiv \tau/\tau' = 1/(1 - \omega P\Delta\Omega), \quad (2)$$

where  $\omega$  is single-scattering albedo and  $P\Delta\Omega$  is a shorthand for the normalized phase function  $P$  integrated over the Sun photometer FOV, i.e.,

$$P\Delta\Omega \equiv \int_0^\eta P(\theta) \sin \theta d\theta / \int_0^\pi P(\theta) \sin \theta d\theta, \quad (3)$$

where  $\theta$  is scattering angle. *Box and Deepak* [1979] obtained the analogous result for nonabsorbing aerosols ( $\omega = 1$ ) by using analytical approximations.

[9] For completeness we note that (2) can be obtained easily using the single-scattering approximation  $\exp(-\tau_{\text{slant}}) = 1 - \tau_{\text{slant}}$ . However, for this paper the important point is that equation (2) actually describes all orders of scattering, over the range  $0 < \tau_{\text{slant}} < 6$ , as shown by the Monte Carlo calculations of *Shiobara and Asano* [1994] and *Kinne et al.* [1997]. It is also important to include the denominator in (3) since the formulations of *Shiobara and Asano* [1994] and *Kinne et al.* [1997] require that  $P\Delta\Omega$  be the fraction of scattered photons with  $\theta < \eta$ , and several normalizations for  $P(\theta)$  are common in the literature (e.g., the denominator in equation (3) is 1 in the study by *Shiobara and Asano* [1994], but 2 in the studies by *Wiscombe and Grams* [1976] and *Dubovik et al.* [2002a]).

#### 3.2. Effect of Mixed Aerosol-Rayleigh Phase Functions and Vertical Profiles

[10] Not emphasized in many of the previous studies of diffuse light corrections is that Rayleigh scattering often makes a significant contribution to optical depth  $\tau$ , especially at the short wavelengths where aerosol phase functions are most forward peaked. Thus  $\omega P\Delta\Omega$ , the fraction of scattered plus absorbed photons with scattering angle  $\theta < \eta$ , has both Rayleigh and aerosol components, written explicitly as

$$\omega P\Delta\Omega = (\omega_a \tau_a P_a \Delta\Omega + \omega_R \tau_R P_R \Delta\Omega) / \tau, \quad (4)$$

where subscripts  $a$  and  $R$  stand for aerosol and Rayleigh, respectively, and

$$\tau = \tau_a + \tau_R. \quad (5)$$

Hence the diffuse light correction factor  $C$  for total optical depth  $\tau$ , given by equations (2) and (4), depends on the

relative contributions of  $\tau_a$  and  $\tau_R$  to  $\tau$ . In a vertical profile, these relative contributions typically vary with height, making  $C$  dependent on height.

[11] However, if we define a correction factor  $C_a$  for aerosol optical depth analogous to equation (2), i.e.,

$$C_a \equiv \tau_a / \tau'_a, \quad (6)$$

we can show that  $C_a$  is independent of  $\tau_a / \tau_R$  for all cases of practical interest. We use the fact that in Sun photometry  $\tau_a$  is obtained by subtracting  $\tau_R$  from the measured total optical depth  $\tau$ , i.e.,

$$\tau_a = \tau - \tau_R, \quad (7)$$

or

$$\tau'_a = \tau' - \tau_R, \quad (8)$$

where  $\tau'_a$  is the apparent aerosol optical depth obtained from the apparent total  $\tau'$ . Substituting equation (2) in equation (7) yields

$$\tau_a = C\tau' - \tau_R = C(\tau'_a + \tau_R) - \tau_R. \quad (9)$$

Inserting equation (9) in equation (6) yields

$$C_a = C + (\tau_R / \tau'_a)(C - 1). \quad (10)$$

Then using equations (8), (2), and (4) in equation (10) and rearranging yields

$$C_a = 1/[1 - \omega_a P_a \Delta\Omega - (\tau_R / \tau_a) P_R \Delta\Omega]. \quad (11)$$

This differs negligibly from

$$C_a = 1/[1 - \omega_a P_a \Delta\Omega] \quad (12)$$

as long as

$$\tau_R / \tau_a \ll \omega_a P_a \Delta\Omega / P_R \Delta\Omega. \quad (13)$$

As we will show, aerosol phase functions  $P_a$  that have significant diffuse light effects typically have  $\omega_a P_a \Delta\Omega > \sim 100 P_R \Delta\Omega$  for typical Sun photometer or pyrheliometer FOVs (i.e.,  $\eta < \sim 3^\circ$ ). In such cases, equation (13) becomes

$$\tau_R \ll 100 \tau_a. \quad (14)$$

We find that equation (14) or the more general equation (13) is satisfied for all significant tropospheric aerosols at altitudes below  $\sim 6$  km for wavelengths between 340 and 1556 nm. For very tenuous aerosols or stratospheric altitudes the more general equation (11) can be used in place of equation (12), but in such conditions other errors, such as uncertainties in Rayleigh subtraction in equations (7) or (8), are likely to dominate any diffuse light errors.

### 4. Results

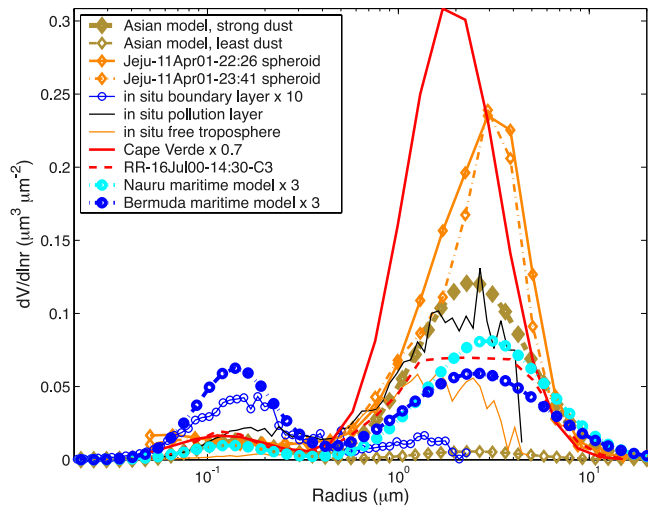
[12] Table 2 lists the aerosol cases for which we have calculated diffuse light correction factors in this study. In selecting these cases our aim has been to cover a wide range

Table 2. Aerosol Measurements and Retrieved Values Used in This Study

Characteristic	$\lambda$ , nm	Asian Dust, AERONET				Asian Aerosol, In Situ				African Dust, AERONET				Maritime Aerosol, AERONET			
		Asian Spheroid Dynamic Model	Jeju 11 April 2250 UT Case 3	Jeju 11 April 2226 UT Spheroid	Jeju 11 April 2341 UT	<i>Wang et al.</i> [2002] Boundary Layer	<i>Wang et al.</i> [2002] Pollution Layer	Free Troposphere Doublet	Cape Verde	10 July 1430 UT Case 3 <sup>a</sup>	RR 16 July 1430 UT Case 3 <sup>a</sup>	RR 21 July 1831 UT Case 3 <sup>a</sup>	Lanai	Nauru	Tahiti	Bermuda Ascension	
		<i>Wang et al.</i> [2002]															
Optical depths and Angstrom coefficients																	
$\tau_a(\lambda)$	1020		0.36	0.35	0.34	0.01	0.30	0.18	0.80	0.24	0.19	0.47					
$\alpha(\lambda, 1020)$	380	0.41–1.85	0.88	0.40	0.43	1.65	0.52	0.03	0.16	0.27	0.28	0.52	1.00	0.31	0.95	1.22	0.89
$\alpha(\lambda, 1020)$	500	0.32–1.95	0.58	0.33	0.38	1.76	0.51	0.02	0.07	0.22	0.20	0.39	0.93	0.20	0.78	1.13	0.75
Complex refractive indices																	
$n(\lambda)$	440	1.50	1.48	1.58	1.60	1.50–1.56 <sup>b</sup>	1.40–1.55 <sup>b</sup>	1.51–1.56 <sup>b</sup>	1.48	1.48	1.48	1.48	1.36	1.36	1.36	1.36	1.36
$n(\lambda)$	670	1.50	1.48	1.55	1.60	1.50–1.56 <sup>b</sup>	1.40–1.55 <sup>b</sup>	1.51–1.56 <sup>b</sup>	1.48	1.48	1.48	1.48	1.36	1.36	1.36	1.36	1.36
$n(\lambda)$	870	1.50	1.48	1.52	1.56	1.50–1.56 <sup>b</sup>	1.40–1.55 <sup>b</sup>	1.51–1.56 <sup>b</sup>	1.48	1.48	1.48	1.48	1.36	1.36	1.36	1.36	1.36
$n(\lambda)$	1020	1.50	1.48	1.50	1.53	1.50–1.56 <sup>b</sup>	1.40–1.55 <sup>b</sup>	1.51–1.56 <sup>b</sup>	1.48	1.48	1.48	1.48	1.36	1.36	1.36	1.36	1.36
$k(\lambda)$	440	0.0025	0.0023	0.0027	0.0036	0.0000	0–0.047 <sup>b</sup>	0–0.0028 <sup>b</sup>	0.0023	0.0023	0.0023	0.0023	0.0015	0.0015	0.0015	0.0015	0.0015
$k(\lambda)$	670	0.0025	0.0007	0.0023	0.0034	0.0000	0–0.047 <sup>b</sup>	0–0.0028 <sup>b</sup>	0.0006	0.0007	0.0007	0.0007	0.0015	0.0015	0.0015	0.0015	0.0015
$k(\lambda)$	870	0.0025	0.0006	0.0026	0.0041	0.0000	0–0.047 <sup>b</sup>	0–0.0028 <sup>b</sup>	0.0006	0.0006	0.0006	0.0006	0.0015	0.0015	0.0015	0.0015	0.0015
$k(\lambda)$	1020	0.0025	0.0006	0.0027	0.0043	0.0000	0–0.047 <sup>b</sup>	0–0.0028 <sup>b</sup>	0.0006	0.0006	0.0006	0.0006	0.0015	0.0015	0.0015	0.0015	0.0015
Single-scattering albedos																	
$\omega_a(\lambda)$	440	see text	0.94	0.92	0.91	1.00	0.81	0.94	0.93	0.94	0.95	0.95	0.97	0.94	0.96	0.98	0.97
$\omega_a(\lambda)$	670	see text	0.98	0.94	0.92	1.00	0.83	0.95	0.98	0.98	0.98	0.99	0.97	0.95	0.96	0.97	0.96
$\omega_a(\lambda)$	870	see text	0.98	0.94	0.92	1.00	0.86	0.96	0.99	0.99	0.99	0.99	0.97	0.96	0.96	0.97	0.97
$\omega_a(\lambda)$	1020	see text	0.98	0.95	0.92	1.00	0.87	0.97	0.99	0.99	0.99	0.99	0.97	0.97	0.96	0.97	0.97
Parameters of column and layer size distributions																	
$r_{Vf}$ , $\mu\text{m}$		0.14	0.08	0.13	0.15	0.15	0.18	0.14	0.13	0.11	0.15	0.12	0.15	0.13	0.12	0.14	0.13
$r_{Vc}$ , $\mu\text{m}$		2.43	2.48	2.53	2.46	1.19	1.74	1.36	1.90	1.86	2.28	1.50	2.74	2.93	3.29	2.55	2.62
$\sigma_{Vf}$		0.47	0.32	0.73	0.70	0.62	0.49	0.41	0.47	0.36	0.54	0.41	0.57	0.49	0.38	0.46	0.40
$\sigma_{Vc}$		0.67	0.58	0.58	0.59	0.31	0.55	0.61	0.56	0.68	0.69	0.54	0.74	0.72	0.78	0.83	0.78
$C_{Vc}$ , $\mu\text{m}^3/\mu\text{m}^2$		0.025–0.22	0.48	0.36	0.32	0.01	0.19	0.10	0.66	0.19	0.17	0.32	0.05	0.05	0.04	0.07	0.09
$C_{Vc}/C_V$		0.39–0.93	0.74	0.92	0.92	0.22	0.85	0.97	0.95	0.88	0.87	0.85	0.71	0.92	0.77	0.63	0.76
$R_{eff}$ , $\mu\text{m}$		0.20–0.97	0.27	0.80	0.81	0.15	0.64	0.89	0.99	0.59	0.67	0.49	0.39	0.94	0.42	0.30	0.42
$R_{diff-f}$ , $\mu\text{m}$		0.13	0.08	0.11	0.12	0.13	0.16	0.13	0.11	0.11	0.13	0.11	0.13	0.12	0.11	0.13	0.12
$R_{diff-c}$ , $\mu\text{m}$		1.94	2.08	2.12	2.05	1.13	1.49	1.13	1.62	1.48	1.81	1.30	2.08	2.26	2.43	1.81	1.93
Diffuse light correction factors																	
$C(0.6^\circ, \lambda)$	440	1.00–1.01	1.01	1.01	1.01	1.000	1.003	1.004	1.01	1.00	1.01	1.00	1.005	1.012	1.008	1.004	1.006
$C(1.85^\circ, \lambda)$	440	1.01–1.07	1.05	1.07	1.06	1.004	1.030	1.037	1.06	1.04	1.05	1.03	1.036	1.091	1.053	1.026	1.042
$C(2.85^\circ, \lambda)$	440	1.02–1.11	1.08	1.12	1.11	1.008	1.055	1.074	1.12	1.08	1.08	1.06	1.060	1.151	1.083	1.043	1.069

<sup>a</sup>RR, Roosevelt Roads Naval Air Station, Puerto Rico.<sup>b</sup>Size dependent.





**Figure 1.** Volume-versus-size distributions for representative aerosol columns and layers selected from Table 2.

of realistic cases of practical interest. Table 2 includes Asian and African aerosols containing varying proportions of dust, as well as maritime aerosols from five island sites. The symbols in the first column of Table 2 are defined as follows:

$\tau_a(\lambda)$	aerosol optical depth at wavelength $\lambda$ ;
$\alpha(\lambda_1, \lambda_2)$	Ångström exponent;
$n, k$	real, imaginary refractive index;
$\omega$	single-scattering albedo;
$r_{Vf}, r_{Vc}$	volume median radius for fine and coarse modes, respectively;
$\sigma_{Vf}, \sigma_{Vc}$	standard deviation about volume median radius, for fine and coarse modes;
$C_V, C_{Vc}$	volume concentration for total distribution and coarse mode, respectively;
$R_{eff-f}, R_{eff-c}$	effective (area-weighted) radius for fine and coarse modes, respectively.

The Ångström exponent above is defined by

$$\alpha(\lambda_1, \lambda_2) \equiv -\ln[\tau_a(\lambda_1)/\tau_a(\lambda_2)]/\ln(\lambda_1/\lambda_2). \quad (15)$$

[13] *Dubovik et al.* [2002a] give equations for computing the above size distribution parameters  $r_{Vi}$ ,  $\sigma_{Vi}$ ,  $C_{Vi}$  for an arbitrary size distribution or a given mode. For convenience these equations are repeated in Appendix A of this paper. We emphasize that neither these equations nor individual AERONET retrievals assume any particular functional form. However, the AERONET retrievals usually yield shapes that are bimodal, a result also found by other studies [e.g., *Whitby, 1978; Shettle and Fenn, 1979; Remer and Kaufman, 1998*].

[14] Figure 1 shows representative column and layer size distributions from Table 2. Note that apart from the distributions labeled “model,” none of the distributions is exactly lognormal, but they are roughly bimodal. This includes both the in situ results of *Wang et al.* [2002] and the individual AERONET retrievals. Applying the equations of *Dubovik et al.* [2002a] (reproduced in our Appendix A) to these distributions yielded the parameters in Table 2.

#### 4.1. Particle Shape and Phase Functions

[15] The maritime aerosol size distributions and complex refractive indices in Table 2 were all derived by *Smirnov et al.* [2002] from AERONET measurements. The Asian aerosol cases include three from airborne in situ measurements by *Wang et al.* [2002] (see also below), plus a variety of retrievals from AERONET measurements. When dust was present during the Asian AERONET measurements, use of spherical particle phase functions had a strong tendency to produce the retrieval artifacts described by *Dubovik et al.* [2002a, 2002b], i.e., an artificially strong small-particle mode and real refractive indices that are artificially small at short wavelengths (sometimes nonphysically small, i.e., less than the real refractive index of water). Therefore most of the Asian aerosol AERONET retrievals were done with spheroidal phase functions [*Mishchenko et al., 1997*], which, as shown by *Dubovik et al.* [2002a, 2002b], produce retrievals without these artifacts. Dust retrievals in Table 2 (both African and Asian) that used spherical phase functions have been screened and adjusted to minimize artifacts (e.g., by checking small-mode amplitude and adjusting short-wavelength real refractive indices to values found for dust retrievals with scattering angles less than  $\sim 30^\circ$ , which are not susceptible to effects of nonsphericity).

[16] We used a large number of AERONET retrievals (all done with spheroidal phase functions) from measurements at Chinhae, Anmyon, Jeju and Seoul in South Korea, and Shirahama and Osaka in Japan, to derive a dynamic model of the mixed Asian aerosol, in which the amplitude of the coarse mode varies to reflect different amounts of dust. Parameters of this Asian dynamic model are summarized in the leftmost Asian dust column of Table 2, and two example columnar size distributions are shown in Figure 1. Other AERONET dust cases are included in our study (Table 2, with examples in Figure 1) to show the degree of variation with respect to the model, which tends to capture average behavior.

[17] Dust nonsphericity also can affect in situ aerosol measurements. For example, in the free troposphere measurements of *Wang et al.* [2002], dust nonsphericity caused particles to be undersized in the aerodynamic particle sizer. *Wang et al.* [2002] corrected this aerodynamic undersizing by modeling the dust particles as doublet spheres (hence the designation “Free Troposphere Doublet” in Table 2). After this correction, *Wang et al.* [2002] found that multiwavelength extinction spectra calculated from the in situ measurements agreed with spectra from airborne Sun photometry [*Schmid et al., 2003*], which is not subject to these aerodynamic sizing issues.

[18] Figure 2 illustrates the similarities and differences between phase functions for spheres and spheroids, in this case for the size distribution retrieved from AERONET Sun-sky measurements at Jeju, Korea, 11 April 2001, 2341 UT. (The retrieval itself used spheroidal phase functions, to obtain the most accurate size distribution.) The results, which are for spheres and spheroids having the same volume-versus-size distribution (plotted in Figure 1, with parameters listed in Table 2), show that phase functions for spheres and equal-volume spheroids can differ significantly for scattering angles  $> 40^\circ$ , but that they are quite similar in the forward scattering peak. Differences between phase

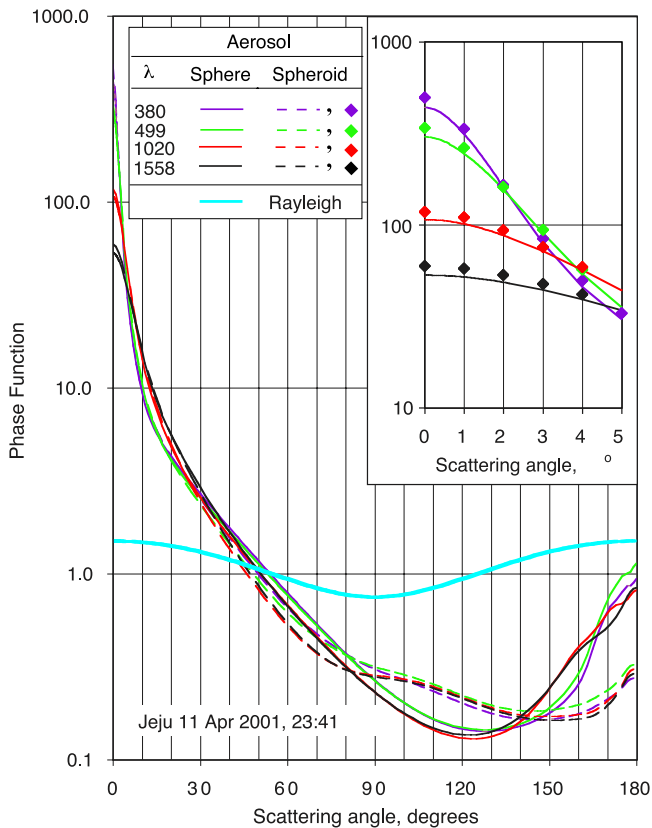


**Figure 2.** Phase functions at selected wavelengths for the aerosol size distribution retrieved from AERONET Sun-sky measurements at Jeju, Korea, 11 April 2001, 2341 UT. The size distribution retrieval assumed spheroidal kernels, using the method of *Dubovik et al.* [2002b]. Aerosol phase functions  $P_a(\theta)$  shown were calculated for this single size distribution, assuming either spheroids or equal-volume spheres. Rayleigh phase function  $P_R(\theta)$  is shown for comparison.

functions for spheres and volume-equivalent spheroids for this case are  $<14\%$  in the forward peak. Also, the forward peak integrals determining diffuse light corrections (e.g., in equation (3)) differ even less (by  $<7\%$  for FOV angles of practical interest), because of the weighting by  $\sin \theta$  in equation (3). Furthermore, when these integrals are used in equation (12) to obtain diffuse light correction factors  $C_a$ , resulting  $C_a$  values for spheres and volume-equivalent spheroids differ by  $<1\%$  for the aerosol cases and FOV angles in this paper. Differences between results for spheres and equal-area spheroids are even less than the differences given here between spheres and equal-volume spheroids.

[19] To summarize, dust nonsphericity can cause significant errors in size distributions determined in situ by aerodynamic methods, as well as significant errors in both size distributions and refractive indices retrieved from AERONET measurements, unless analysis methods account for this nonsphericity. However, once accurate size distribution and complex refractive index have been determined by suitable analyses, the use of spherical-particle phase functions in equation (3) can produce accurate diffuse light corrections, because of the similarity between

spherical and nonspherical phase functions in the forward peak. In this paper, we have followed this approach. That is, we have used analysis methods that produce accurate size distribution and complex refractive index for particles that may be nonspherical, and then used spherical-particle phase functions in the forward peak to calculate diffuse light effects.

[20] Figure 2 and the above discussion of phase functions are based on using a model of spheroids (ellipsoids of revolution) to represent nonspherical particles. Recently, *Kalashnikova and Sokolik* [2002] have shown that dust particles with angular, sharp-edged shapes have phase functions with forward peaks as much as 1.5 times those of volume-equivalent spheres. We have not used the phase functions of such angular, sharp-edged particles in this study, partly because of the computational burden, but also because of a variety of evidence that dust particles in the atmosphere, especially at significant distances from their sources, may scatter light more like spheroids than angular, sharp-edged particles. This evidence includes (1) results showing that dust particles often acquire coatings (e.g., sulfates or organics) as they are transported downwind [e.g., *Krueger et al.*, 2003], and (2) consistency between dust characteristics retrieved assuming spheroidal phase functions and determined by other means [e.g., *Sinyuk et al.*, 2003]. However, when evaluating diffuse light effects of dust near sources, where angular, sharp-edged shapes are likely to be more dominant, it may be appropriate to adjust the results of this study to account for these shapes (e.g., by increasing  $C_a - 1$  by as much as 50%, to account for the factor 1.5 forward peak difference noted above). See also section 5.

#### 4.2. Diffuse Light Correction Factors

[21] Using equations (12) and (3), we have calculated diffuse light correction factors  $C_a(\lambda, \eta)$  for each of the

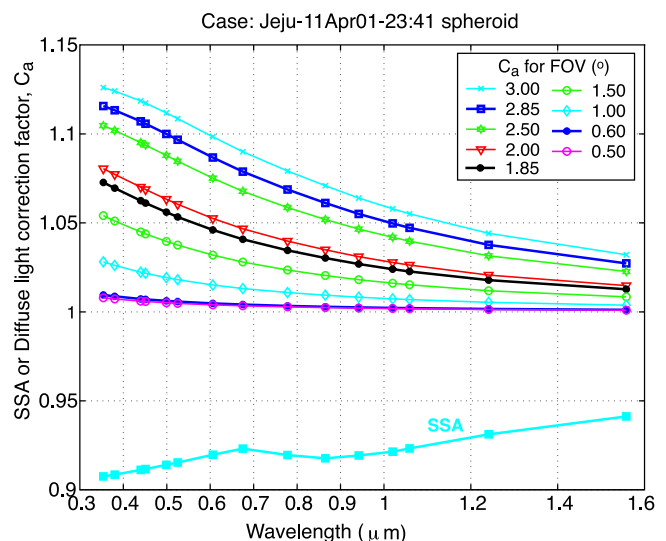


**Figure 3.** Single-scattering albedo SSA and diffuse light correction factors  $C_a$  for the aerosol size distribution retrieved from AERONET Sun-sky measurements at Jeju, Korea, 11 April 2001, 2341 UT. This case has  $\alpha(380, 1020) = 0.429$ ,  $\alpha(1020, 1558) = 0.091$ .

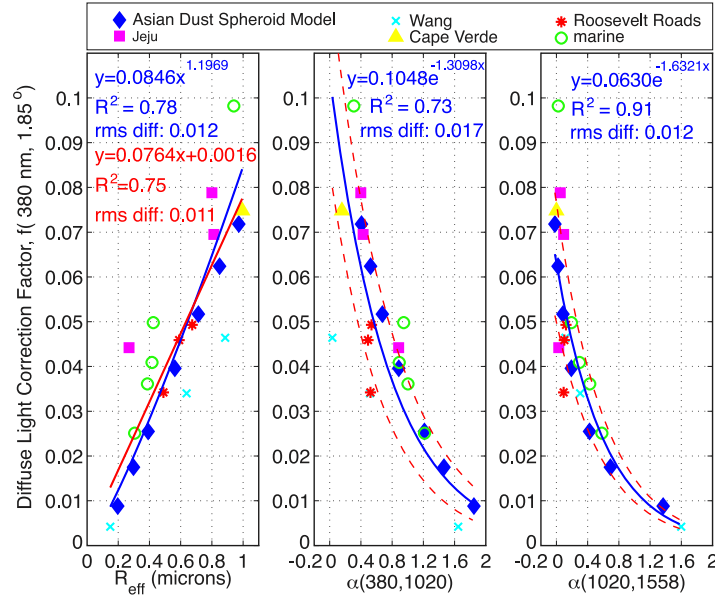


**Figure 4.** Scatterplots of correction factors  $f$  versus  $R_{\text{eff}}$  and Ångström exponents, with fitting equations and measures of fit. Short-dashed lines in the middle and right frames show RMS deviation of points from fit.

aerosol cases in Table 2, for wavelengths  $\lambda = 354$  to 1558 nm and FOV half-angles  $\eta = 0.5^\circ$  to  $3.0^\circ$ . Figure 3 illustrates the dependence of  $C_a$  on  $\lambda$  and  $\eta$ , for the same case as used in the phase function examples of Figure 2 (i.e., size distribution and complex refractive indices retrieved from AERONET Sun-sky measurements at Jeju, Korea, 11 April 2001, 2341 UT, listed in the fourth column of Asian dust in Table 2). Also shown is single-scattering albedo SSA, which affects  $C_a$  via equation (12). The increase in  $C_a$  with decreasing wavelength is caused by the increased forward peaking of phase functions with decreasing wavelength, shown in Figure 2. However, this increase can be reduced or even reversed if SSA decreases fast enough with decreasing wavelength (compare equation (12)). FOV half-angles  $\eta$  for specific instruments are shown by heavy lines in Figure 3; i.e., (1)  $\eta = 0.6^\circ$  for the AERONET Cimel Sun-sky photometers [Holben *et al.*, 1998; Eck *et al.*, 1999], (2)  $\eta = 1.85^\circ$  for the NASA Ames airborne Sun photometers (AATS-6 and AATS-14 [e.g., Livingston *et al.*, 2003; Redemann *et al.*, 2003; Schmid *et al.*, 2003]), and (3)  $\eta = 2.85^\circ$  for the normal incidence pyranometer (NIP) [Halthore *et al.*, 1997].

[22] The results for  $C_a$  and SSA shown in Figure 3 and elsewhere in this study use the complex refractive indices shown in Table 2, linearly interpolated between the four wavelengths used in AERONET retrievals, 440, 670, 870, and 1020 nm. For shorter wavelengths (i.e., at 354 and 380 nm), complex refractive index was linearly extrapolated. For longer wavelengths (i.e., at 1059, 1241, and 1558 nm), complex refractive index was set equal to that at the nearest limit of AERONET retrieval wavelengths (i.e., 1020 nm). This extension of complex refractive index introduces little uncertainty into  $C_a$ , because the extension in the UV (from 440 to 354 nm) covers a relatively small wavelength interval, and because  $C_a$  values are themselves relatively small in the IR extension region (1020–1558 nm). However, it does

introduce significant uncertainty into Ångström exponents that have one or both wavelengths in the IR extension region. This is discussed further in section 5.

#### 4.3. Correlation of Diffuse Light Correction Factors With $R_{\text{eff}}$ and Ångström Exponents

[23] Results for diffuse light correction factors  $C_a(\lambda, \eta)$  for  $\lambda = 440$  nm and the above three  $\eta$  values are shown in the lower rows of Table 2. Figure 4 shows results for  $\lambda = 380$  nm,  $\eta = 1.85^\circ$  as scatterplots versus several parameters. For convenience of display these are shown as

$$f \equiv C_a - 1. \quad (16)$$

Different groups of aerosols from Table 2 are plotted with different symbols in Figure 4, to aid in showing whether different groups have significantly different relationships to the parameters plotted on the  $x$  axes. (See also section 5.)

[24] The left frame of Figure 4 shows that  $f(380 \text{ nm}, 1.85^\circ)$  (and hence  $C_a(380 \text{ nm}, 1.85^\circ)$ ) is correlated with  $R_{\text{eff}}$ . The square of the correlation coefficient,  $R^2$ , is 0.75 and 0.78 for linear and power law fits, respectively. ( $R^2$  is the fraction of the variance that is accounted for by the fit [e.g., Edwards, 1976]. Figure C-3 of Bevington [1969] shows that the probability of obtaining such large values of  $R^2$  from an uncorrelated population with  $N = 22$  is  $<0.001$ .) Thus, within the set of aerosol cases in Table 2, knowledge of  $R_{\text{eff}}$  can be used to determine  $C_a(380 \text{ nm}, 1.85^\circ)$  with useful accuracy (RMS deviation of data points from the linear and power law fits is 0.011 and 0.012, respectively). Unfortunately, in most Sun photometer measurements,  $R_{\text{eff}}$  of the viewed aerosol is not known. However, the Ångström exponent, defined by equation (15) above, can be determined directly from a Sun-photometer-measured spectrum  $\tau_a(\lambda)$ , and it is known to be an indicator of aerosol size. Therefore, in the remaining frames of Figure 4 we show

**Table 3.** Parameters of Best Fit Curves  $f(\lambda, \eta) = A \exp [B \alpha(\lambda_1, \lambda_2)]$  and of RMS Deviations From Fit  $\delta f = f^*[a + b\alpha(\lambda_1, \lambda_2)]$ 

$\lambda, \text{nm}$	$\lambda_1, \lambda_2 = 380, 1020 \text{ nm}$											
	$\eta = 0.6^\circ$				$\eta = 1.85^\circ$				$\eta = 2.85^\circ$			
	$A$	$B$	$a$	$b$	$A$	$B$	$a$	$b$	$A$	$B$	$a$	$b$
354	0.0143	-1.3229	0.3090	0.0798	0.1109	-1.3502	0.1932	0.1076	0.1833	-1.3291	0.1463	0.1039
380	0.0129	-1.2616	0.3138	0.0745	0.1048	-1.3098	0.1990	0.1107	0.1773	-1.2966	0.1516	0.1081
449	0.0103	-1.1748	0.2998	0.1048	0.0900	-1.2008	0.2048	0.1258	0.1605	-1.2062	0.1560	0.1319
499	0.0089	-1.0792	0.3012	0.1034	0.0807	-1.1211	0.2091	0.1324	0.1479	-1.1317	0.1619	0.1398
525	0.0082	-1.0312	0.2958	0.1081	0.0759	-1.0751	0.2099	0.1347	0.1410	-1.0896	0.1634	0.1438
606	0.0064	-0.8833	0.2968	0.1078	0.0626	-0.9384	0.2159	0.1411	0.1203	-0.9606	0.1707	0.1543
675	0.0054	-0.7837	0.2892	0.1112	0.0533	-0.8336	0.2199	0.1461	0.1045	-0.8534	0.1789	0.1571
778	0.0041	-0.6320	0.2858	0.1119	0.0421	-0.6846	0.2252	0.1465	0.0845	-0.7062	0.1879	0.1588
865	0.0033	-0.5268	0.2812	0.1148	0.0348	-0.5685	0.2326	0.1409	0.0710	-0.5932	0.1974	0.1548
940	0.0028	-0.4307	0.2804	0.1114	0.0297	-0.4806	0.2400	0.1342	0.0612	-0.5039	0.2063	0.1483
1019	0.0024	-0.3678	0.2681	0.1136	0.0257	-0.4146	0.2405	0.1352	0.0534	-0.4332	0.2110	0.1462
1059	0.0023	-0.3921	0.2690	0.1373	0.0239	-0.3777	0.2423	0.1322	0.0499	-0.3956	0.2126	0.1437
1241	0.0017	-0.2628	0.2566	0.1349	0.0179	-0.2529	0.2422	0.1246	0.0379	-0.2698	0.2175	0.1352
1558	0.0011	-0.1142	0.2639	0.1100	0.0122	-0.1204	0.2388	0.1096	0.0261	-0.1292	0.2223	0.1151

$\lambda, \text{nm}$	$\lambda_1, \lambda_2 = 1020, 1558 \text{ nm}$											
	$\eta = 0.6^\circ$				$\eta = 1.85^\circ$				$\eta = 2.85^\circ$			
	$A$	$B$	$a$	$b$	$A$	$B$	$a$	$b$	$A$	$B$	$a$	$b$
354	0.0088	-1.7573	0.3028	0.0048	0.0648	-1.6408	0.2115	-0.0087	0.1057	-1.5441	0.2124	-0.0451
380	0.0082	-1.7088	0.3139	0.0027	0.0630	-1.6321	0.2108	-0.0004	0.1048	-1.5434	0.1938	-0.0338
449	0.0071	-1.7011	0.3248	0.0552	0.0582	-1.5986	0.2239	0.0245	0.1015	-1.5366	0.1847	-0.0021
499	0.0064	-1.6215	0.3341	0.0531	0.0548	-1.5563	0.2357	0.0391	0.0980	-1.5024	0.1944	0.0073
525	0.0060	-1.5781	0.3410	0.0496	0.0329	-1.5238	0.2443	0.0330	0.0958	-1.4786	0.2014	0.0106
606	0.0051	-1.4453	0.3552	0.0454	0.0471	-1.4277	0.2669	0.0511	0.0882	-1.3995	0.2231	0.0384
675	0.0044	-1.3465	0.3644	0.0447	0.0425	-1.3483	0.2808	0.0752	0.0811	-1.3183	0.2399	0.0546
778	0.0036	-1.1918	0.3708	0.0477	0.0361	-1.2113	0.2996	0.0912	0.0708	-1.1940	0.2613	0.0804
865	0.0031	-1.0747	0.3660	0.0550	0.0314	-1.0945	0.3093	0.1304	0.0627	-1.0860	0.2733	0.0987
940	0.0027	-0.9706	0.3721	0.0559	0.0279	-0.9999	0.3164	0.1096	0.0563	-0.9942	0.2825	0.1065
1019	0.0024	-0.8891	0.3652	0.0662	0.0249	-0.9344	0.3185	0.1363	0.0508	-0.9220	0.2865	0.1318
1059	0.0023	-0.9765	0.3608	0.1932	0.0235	-0.8910	0.3200	0.1411	0.0482	-0.8805	0.2897	0.1349
1241	0.0017	-0.7944	0.3441	0.2187	0.0185	-0.7391	0.3236	0.1524	0.0386	-0.7345	0.2963	0.1558
1558	0.0012	-0.5836	0.3544	0.1886	0.0132	-0.5490	0.3220	0.1491	0.0279	-0.5416	0.3033	0.1450

scatterplots of  $f(380 \text{ nm}, 1.85^\circ)$  versus Ångström exponent for two wavelength pairs: 380, 1020 nm (middle frame) and 1020, 1558 nm (right frame). Also shown are exponential best fit curves of the form

$$f = C_a - 1 = A \exp(-B\alpha). \quad (17)$$

Notice that the correlation between  $f(380 \text{ nm}, 1.85^\circ)$  and  $\alpha(380 \text{ nm}, 1020 \text{ nm})$ ,  $R^2 = 0.73$  (middle frame), is similar to that between  $C_a(380 \text{ nm}, 1.85^\circ)$  and  $R_{\text{eff}}$  (left frame). Moreover, the correlation is even stronger ( $R^2 = 0.91$ , right frame) versus Ångström exponent at the longer-wavelength pair,  $\alpha(1020 \text{ nm}, 1558 \text{ nm})$ . This is an example of a general result of our calculations: that the correction factors were well correlated with Ångström exponent and that the correlation improved as wavelengths  $\lambda_1$  and  $\lambda_2$  increased. (Evidently, this is because longer wavelengths are more sensitive to the larger particles in a distribution, and the larger particles are responsible for the diffuse light effects.)

#### 4.4. Parameters of Fitting Equations for Correction Factors

[25] The results in Figure 4 suggest a method for determining the most appropriate correction factors  $C_a(\lambda, \eta)$  to apply to a given Sun photometer measurement,  $\tau_a(\lambda)$ . That is, determine best fit equations for scatterplots analogous to the middle and right frames of Figure 4 for the appropriate  $\lambda$  and  $\eta$ , and use those equations with  $\alpha(\lambda_1, \lambda_2)$  of the measured  $\tau_a(\lambda)$ . We have done this for the wavelength

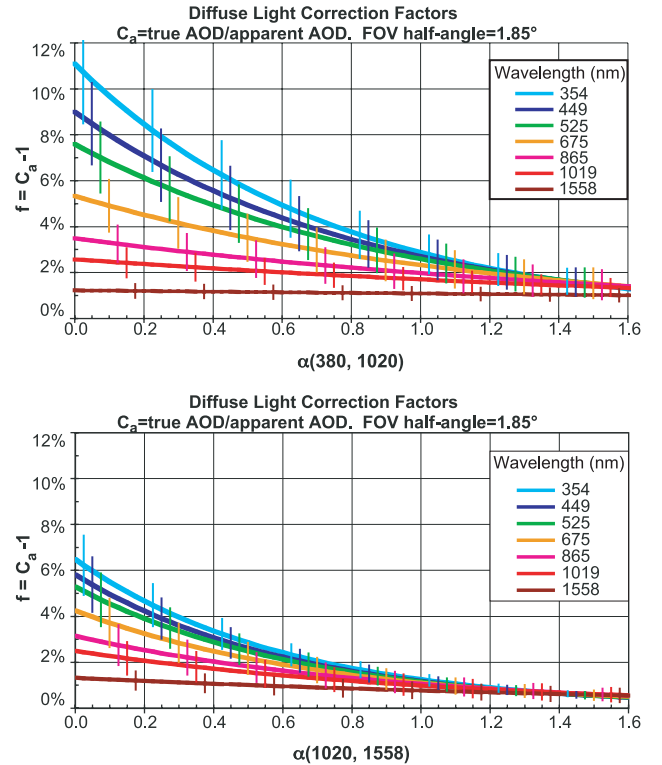


**Figure 5.** Fits of  $C_a - 1$  versus alpha. Vertical bars show  $\pm 1$  RMS deviation of individual cases from fit.



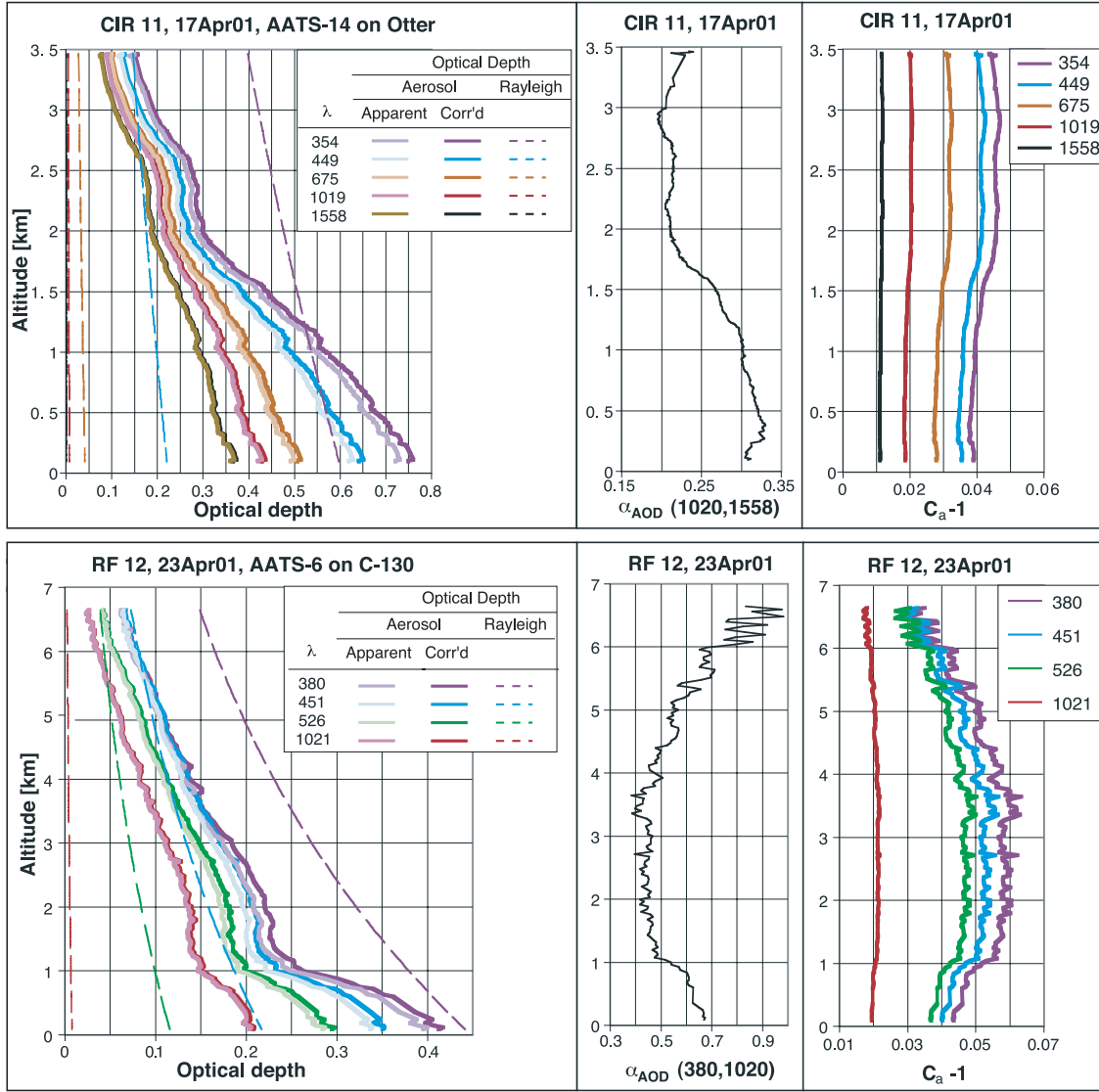


**Figure 6.** Examples of applying the diffuse light correction factors in Table 3 and Figure 5 to vertical profiles of optical depth measured in ACE-Asia.

range 354–1556 nm. Table 3 lists the best fit parameters of the fitting equation (17). Also given are the RMS deviations of the data points from the fit, which indicate the  $1\sigma$  uncertainty of this approach. These diffuse light uncertainties can be included in the overall AOD uncertainty by using equation (A22b) of Russell *et al.* [1993a]. Figure 5 shows these best fit curves for  $\eta = 1.85^\circ$ , which is the FOV half-angle of the NASA Ames airborne Sun photometers (AATS-6 and AATS-14). At  $\lambda = 1558$  nm these corrections are  $<1\%$  of AOD for all  $\alpha$ . However, for the shorter wavelengths and smaller  $\alpha$  values they are significant, ranging up to 10% of AOD for  $\lambda = 354$  nm and  $\alpha(380 \text{ nm}, 1020 \text{ nm}) = 0$ .

[26] Because  $f$  and  $C$  decrease with increasing wavelength, applying these corrections to an apparent AOD spectrum,  $\tau'_a(\lambda)$ , changes its slope, increasing its Ångström exponents (i.e.,  $\alpha(\lambda_1, \lambda_2) > \alpha'(\lambda_1, \lambda_2)$ , where  $\alpha'$  and  $\alpha$  are the Ångström exponents of the apparent and corrected AOD spectra,  $\tau'_a(\lambda)$ ,  $\tau_a(\lambda)$ , respectively. This raises the question of whether the correction made using an initial, apparent Ångström

exponent  $\alpha(\lambda_1, \lambda_2)$  is an overcorrection, and whether it is necessary to iterate using the Ångström exponent of the corrected AOD spectrum. We have conducted such iterative solutions for example cases. In all cases we found that iteration was not necessary, because the first corrected spectrum,  $\tau_a(\lambda)$ , was virtually identical to the spectrum found in all subsequent iterations (AOD differences  $< 0.001$ ).

#### 4.5. Applications

[27] Figure 6 illustrates the application of the correction factors in Table 3 and Figure 5 to vertical profiles of apparent AOD  $\tau'_a(\lambda)$  measured in ACE-Asia. The top row is a case measured by the 14-channel Ames Airborne Tracking Sunphotometer (AATS-14) on the Twin Otter aircraft; the bottom row is from measurements by its 6-channel counterpart, AATS-6 on the C-130 aircraft. In ACE-Asia, the prevalence of dust relative to smaller aerosol particles tended to increase with altitude. This is reflected in the vertical profiles of Ångström exponent shown in the middle frame of each row: Ångström exponent generally

decreases in going from the near-surface pollution layer ( $\sim 0.3$  km to 1 or 2 km) to the layer 1 or 2 km above. In addition, the 17 April 2001 example in the top row of Figure 6 shows Ångström exponent decreasing in moving downward from  $\sim 0.3$  km and 0.1 km, possibly because of a near-surface layer with enhanced sea salt. The vertical profiles of Ångström exponent in each row of Figure 6 were used with the coefficients of Table 3 (equivalently, the curves of Figure 5) to obtain the vertical profiles of correction factors shown in the right frame of each row of Figure 6. Applying these correction factor profiles to the profiles of apparent AOD  $\tau'_a(\lambda)$  in the left frames yields the corresponding profiles of corrected AOD  $\tau_a(\lambda)$  also shown in the left frames.

[28] In ACE-Asia, dust frequently occurred with pollution, even in the same layers aloft. Hence effective radii were usually smaller, and Ångström coefficients larger, than would be the case for pure dust. This is reflected by the Ångström exponent profiles in Figure 6: The minimum Ångström exponents attained are  $\alpha(1020 \text{ nm}, 1558 \text{ nm}) = \sim 0.2$  and  $\alpha(380 \text{ nm}, 1020 \text{ nm}) = \sim 0.4$ . Hence the maximum correction factors  $C_a - 1$  are  $\sim 5\%$  of AOD at the shortest wavelengths. Although these are less than the  $C_a - 1$  values of  $\sim 6\text{--}10\%$  for the smallest Ångström exponents in Figure 5, they nevertheless produce AOD changes that are clearly evident in Figure 6 for the shorter wavelengths at altitudes below  $\sim 3\text{--}4$  km. For example, at wavelength 354 nm below  $\sim 0.5$  km in the top row of Figure 6, the diffuse light correction increases AOD by  $\sim 0.03$ . This is significant compared to the typical AOD uncertainty of  $\sim 0.01\text{--}0.02$  in well-calibrated Sun photometer measurements.

[29] Rayleigh optical depths  $\tau_R$  are shown in Figure 6 along with the aerosol optical depths  $\tau_a$ . This is to illustrate the point made in section 3.2, that  $\tau_R$  is small compared to  $100\tau_a$  for altitudes below  $\sim 6$  km for wavelengths as short as 340 nm. Hence the approximation of equation (12) for  $C_a$  is valid.

[30] Analogous diffuse light corrections have been applied by *Livingston et al.* [2003] to AODs obtained by AATS-6 in the Puerto Rico Dust Experiment (PRIDE) and by *Redemann et al.* [2003] and *Schmid et al.* [2003] to AODs obtained by AATS-6 and AATS-14 in the Asian-Pacific Regional Aerosol Characterization Experiment (ACE-Asia). The PRIDE measurements focused on Saharan dust aerosols transported across the Atlantic to the Caribbean. Diffuse light correction factors were based on a limited set of aerosol size distributions and complex refractive indices: essentially the cases under the header “African Dust, AERONET” in Table 2. Despite the exclusion of the other cases in Table 2 (i.e., Asian dust and Asian mixed aerosols, plus maritime aerosols), the correction factors applied to the PRIDE AODs were very similar to those found here for the PRIDE range of  $\alpha(380 \text{ nm}, 1020 \text{ nm})$ :  $\sim 0.2\text{--}0.5$ . Values of  $C_a - 1$  ranged from a maximum of  $\sim 6\%$  at 380 nm to a minimum of  $\sim 2\%$  at 1021 nm [*Livingston et al.*, 2003]. The diffuse light correction factors applied to ACE-Asia AODs by *Redemann et al.* [2003] and *Schmid et al.* [2003] were based on a larger subset of aerosol columnar size distributions and complex refractive indices: essentially all the cases in Table 2 except those under the header “Maritime Aerosol, AERONET.” Both Saharan and Asian aerosols were included because we

found no significant, systematic differences between the  $f$ -versus- $\alpha$  scatterplots for the two, and we sought a robust relationship applicable to dust and mixed dust-pollution aerosols from both sources.

[31] For the study reported here, we sought a relationship still more widely applicable, to both dust and maritime aerosols. Therefore we extended the data set further, to include the cases headed “Maritime Aerosol, AERONET” in Table 2, which use columnar size distributions and complex refractive indices found by *Smirnov et al.* [2002]. Inspection of Figure 4 suggests that inclusion of the maritime cases increases the best fit curves of  $f$ -versus- $\alpha$ , with the increase larger for  $f$ -versus- $\alpha(380, 1020)$  (middle frame of Figure 4) than for  $f$ -versus- $\alpha(1020, 1558)$  (right frame of Figure 4). To quantify this increase, we have solved for the best fit  $f$ -versus- $\alpha$  curves with and without the inclusion of the maritime cases. We found differences  $< 0.012$  in  $f(354 \text{ nm})$ -versus- $\alpha(380, 1020)$ ,  $< 0.003$  in  $f(354 \text{ nm})$  versus- $\alpha(1020, 1558)$ , and still smaller at all longer wavelengths. All differences between best fit curves were less than the RMS difference between individual points and best fit curves. (These RMS differences are shown by the short-dashed curves in Figure 4 and the error bars in Figure 5.) For AODs less than 0.8 the differences between best fit curves produce AOD differences less than the typical Sun photometer AOD measurement uncertainty of 0.01–0.02. Therefore we have retained the combination of dust and maritime cases, and we recommend using the resulting best fit curves (shown in Figure 5, with parameters listed in Table 3) for either dust or maritime cases.

## 5. Discussion and Cautions

[32] We mentioned in section 2 that the coarse mode of dust and maritime aerosols typically has  $R_{\text{eff}} = 1.1\text{--}3.2 \mu\text{m}$ , a range that falls into a gap between results of the previous studies cited in section 1 and listed in Table 1. (These previous results were  $R_{\text{eff}} = 0.2\text{--}0.9 \mu\text{m}$  for aerosol and  $R_{\text{eff}} = 6\text{--}177 \mu\text{m}$  for cloud). Indeed, the coarse modes of the aerosol cases included in this study fall into this gap (see the  $R_{\text{eff-c}}$  row of Table 2, which has values from 1.13 to  $2.43 \mu\text{m}$ ). Notice, however, that the presence of the fine mode causes  $R_{\text{eff}}$  of the overall distribution to be considerably less than that of the coarse mode. This can be seen from the  $R_{\text{eff}}$  row of Table 2 and the horizontal coordinates of the points in the left frame of Figure 4: Overall  $R_{\text{eff}}$  values range from 0.15 to 0.99.  $R_{\text{eff}}$  of the overall distribution is a good predictor of  $C_a$  (see the left frame of Figure 4). Therefore the presence of the fine mode significantly reduces the diffuse light effect below what it would be if only the coarse mode were present. Figure 1 shows that this bimodality is a persistent feature of both the in situ and AERONET-retrieved size distributions. Its effect in reducing diffuse light effects is noteworthy.

[33] Considerations of effective radius are also important in distinguishing between diffuse light effects for clouds and for aerosols. Both  $R_{\text{eff}}$  and  $C$  values for clouds are much larger than those found in this study for dust and maritime aerosols. We caution that the approach of using Ångström exponent  $\alpha$  to predict  $C$  (as in Figure 5, in the middle and right frames of Figure 4, and in Table 3) will fail for clouds. This is because clouds will have  $\alpha \approx 0$ , but cloud  $C$  values

will be much larger than predicted by the  $f$ -versus- $\alpha$  relationships in Figures 4 and 5 and Table 3.

[34] We also caution that our  $f$ -versus- $\alpha(1020, 1558)$  relationships are dependent on our adoption of a wavelength-independent complex refractive index over the range 1020–1558 nm. We made this assumption because of a scarcity of information on typical wavelength dependence of complex refractive index in this region. Better refractive index information is needed in this region. However, we did not make such an assumption in calculating our  $f$ -versus- $\alpha(380, 1020)$  relationships, instead using complex refractive indices either from AERONET retrievals [Dubovik *et al.*, 2002a, 2002b; Smirnov *et al.*, 2002] or from chemical information [Wang *et al.*, 2002]. We have found that using our  $f$ -versus- $\alpha(380, 1020)$  relationships gives very similar results to using our  $f$ -versus- $\alpha(1020, 1558)$  relationships (i.e., the resulting  $f$  values differ by  $<0.03$ , with very rare exceptions). This is because all the dust-containing cases used to calculate those relationships have curved spectra of  $\ln$  AOD versus  $\ln \lambda$ , with  $\alpha(1020, 1558) < \alpha(380, 1020)$ , and we find this same relationship,  $\alpha(1020, 1558) < \alpha(380, 1020)$ , for our ACE-Asia AATS-14 measurements of AOD, again with very rare exceptions [Schmid *et al.*, 2003; B. Schmid, personal communication, 2003]. This same curvature of dust AOD spectra was previously found by Eck *et al.* [1999] in the wavelength range 380–1020 nm. The attraction of the  $f$ -versus- $\alpha(1020, 1558)$  relationships is that they have smaller RMS deviation of individual cases from the best fit curves (Figures 4 and 5). However, this must be balanced by the above caution about unknown refractive index wavelength dependence over the range 1020–1558 nm.

[35] Another caution relating to unknown refractive index wavelength dependence concerns the upper limit of the amplitude of the coarse-particle mode. Specifically, in using the dynamic model of Asian dust given by the first Asian dust column of Table 2, we limited the maximum ratio of coarse-to-total volume,  $C_V/C_V$ , to 0.93. We did this because larger ratios, coupled with wavelength-independent complex refractive index between 1020 and 1558 nm, produced computed AOD spectra that curved upward between those wavelengths (i.e.,  $\alpha(1020, 1558) < -0.02$ ), and we have rarely measured such spectra. However, it is possible that those same size distributions, with  $C_V/C_V > 0.93$ , coupled with a wavelength-dependent complex refractive index, could yield  $\alpha(1020, 1558) > \sim 0$ , in accord with the AOD spectra measured by AATS-14. Such size distributions would have larger  $C_a$  than those shown in Figures 4–6 and Table 3. Again we emphasize that systematic refractive index measurements are needed at wavelengths  $>1020$  nm.

[36] Finally, we repeat the caution noted in section 4.1: When evaluating diffuse light effects of dust near sources, where angular, sharp-edged shapes are likely to be more dominant, it may be appropriate to adjust the results of this study to account for these shapes (e.g., by increasing  $C_a - 1$  by as much as 50%, to account for the forward peak difference noted by Kalashnikova and Sokolik [2002]).

## 6. Summary and Conclusions

[37] The relatively large size of desert dust and maritime aerosols makes Sun photometry of these aerosols more subject to diffuse light effects than is the case for smaller

aerosols. We have calculated AOD correction factors  $C_a$  for these effects, by applying the analytical expression of Shiobara and Asano [1994] and Kinne *et al.* [1997] to a wide range of aerosol size distributions and complex refractive indices, using a range of photometer FOV half-angles  $\eta$  and wavelengths  $\lambda$  which are representative of a set of currently operational Sun photometers and pyrhemometers. The size distributions and complex refractive indices are based on a wide range of retrievals from AERONET measurements, plus several cases from in situ airborne measurements. Effects of dust nonsphericity have been taken into account to obtain accurate size distributions and refractive indices. Having obtained these accurate size distributions, we calculated diffuse light correction factors using spherical-particle phase functions, because of the similarity of these phase functions to those of spheroidal particles in the forward scattering peak. However, we caution that results may have to be increased if the aerosol is dominated by the angular, sharp-edged shapes studied by Kalashnikova and Sokolik [2002]. This is more likely to occur near dust sources, before dust particles have acquired coatings of sulfate, organics, or other materials.

[38] We found that the correction factors were well correlated with Ångström exponent  $\alpha(\lambda_1, \lambda_2)$ , and that the correlation improved as wavelengths  $\lambda_1$  and  $\lambda_2$  increased. Evidently this is because longer wavelengths are more sensitive to the larger particles in a distribution, and the larger particles are responsible for the diffuse light effects. We found that the correction factors for Asian mixed dust-pollution aerosols, when arrayed as a function of Ångström exponent, did not differ significantly from those for Saharan dust, or even for maritime aerosols (both similarly arrayed). These size distributions have coarse modes with effective radii ranging from 1.1 to 2.4  $\mu\text{m}$ . However, the persistent presence of a fine-particle mode significantly reduces the effective radius of the overall distribution, with corresponding reductions in diffuse light correction factors.

[39] We find that the corrections are negligible (less than  $\sim 1\%$  of AOD) for Sun photometers with narrow FOV (half-angle  $\eta < \sim 1^\circ$ ), but that they can be as large as 10% of AOD at 354 nm wavelength for Sun photometers with  $\eta = 1.85^\circ$ . For pyrhemometers (which can have  $\eta$  up to  $\sim 2.8^\circ$ ), corrections can be as large as 16% at 354 nm. We find that AOD correction factors are well correlated with AOD wavelength dependence (hence Ångström exponent). We have provided best fit equations for determining correction factors from Ångström exponents of uncorrected AOD spectra, and we demonstrate their application to vertical profiles of multiwavelength AOD.

## Appendix A: Equations Used to Calculate Size Distribution Parameters

[40] Volume median radius (mean logarithm of the radius), computed for both fine and coarse modes, is

$$\ln r_V = \frac{\int_{r_{\min}}^{r_{\max}} \ln r \frac{dV(r)}{d \ln r} d \ln r}{\int_{r_{\min}}^{r_{\max}} \frac{dV(r)}{d \ln r} d \ln r}, \quad (\text{A1})$$



where  $dV(r)/d\ln r$  is the distribution of a given mode, and  $r_{\min}$  and  $r_{\max}$  are the limits of that mode. Standard deviation about the volume median radius is

$$\sigma_V = \sqrt{\frac{\int_{r_{\min}}^{r_{\max}} (\ln r - \ln r_V)^2 \frac{dV(r)}{d\ln r} d\ln r}{\int_{r_{\min}}^{r_{\max}} \frac{dV(r)}{d\ln r} d\ln r}}. \quad (\text{A2})$$

Volume concentration ( $\mu\text{m}^3/\mu\text{m}^2$ ) is

$$C_V = \int_{r_{\min}}^{r_{\max}} \frac{dV(r)}{d\ln r} d\ln r. \quad (\text{A3})$$

These equations are general in that their formulation does not assume any function for the size distribution  $dV(r)/d\ln r$ . Nevertheless, they are formulated so that they give the parameters of a lognormal size distribution if  $dV(r)/d\ln r$  is a true lognormal, i.e., if, for a given mode,

$$\frac{dV(r)}{d\ln r} = \frac{C_V}{\sqrt{2\pi}\sigma_V} \exp\left[-\frac{(\ln r - \ln r_V)^2}{2\sigma_V^2}\right]. \quad (\text{A4})$$

[41] **Acknowledgments.** This research was supported by NASA's Earth Observing System Inter-Disciplinary Science (EOS-IDS) Program, NASA's Radiation Sciences Program, and the National Oceanic and Atmospheric Administration's Aerosol-Climate Interactions Program. Key portions were conducted as part of the Asian Pacific Regional Aerosol Characterization Experiment (ACE-Asia).

## References

- Bevington, P. R. (1969), *Data Reduction and Error Analysis for the Physical Sciences*, McGraw-Hill, New York.
- Box, M. A., and A. Deepak (1979), Atmospheric corrections to solar radiometry, *Appl. Opt.*, **12**, 1941–1949.
- Chiapello, I., J. M. Prospero, J. R. Herman, and N. C. Hsu (1999), Detection of mineral dust over the North Atlantic Ocean and Africa with the Nimbus 7 TOMS, *J. Geophys. Res.*, **104**, 9277–9291.
- Dubovik, O., and M. D. King (2000), A flexible inversion algorithm for retrieval of aerosol optical properties from Sun and sky radiance measurements, *J. Geophys. Res.*, **105**, 20,673–20,696.
- Dubovik, O., B. N. Holben, T. F. Eck, A. Smirnov, Y. J. Kaufman, M. D. King, D. Tanré, and I. Slutsker (2002a), Variability of absorption and optical properties of key aerosol types observed in worldwide locations, *J. Atmos. Sci.*, **59**, 590–608.
- Dubovik, O., B. N. Holben, T. Lapyonok, A. Sinyuk, M. I. Mishchenko, P. Yang, and I. Slutsker (2002b), Non-spherical aerosol retrieval method employing light scattering by spheroids, *Geophys. Res. Lett.*, **29**(10), 1415, doi:10.1029/2001GL014506.
- Eck, T. F., B. N. Holben, J. S. Reid, O. Dubovik, A. Smirnov, N. T. O'Neill, I. Slutsker, and S. Kinne (1999), Wavelength dependence of the optical depth of biomass burning, urban, and desert dust aerosols, *J. Geophys. Res.*, **104**, 31,333–31,349.
- Edwards, A. L. (1976), The correlation coefficient, in *An Introduction to Linear Regression and Correlation*, chap. 4, pp. 33–46, W. H. Freeman, New York.
- Grassl, H. (1971), Calculated circumsolar radiation as a function of aerosol type, field of view, wavelength, and optical depth, *Appl. Opt.*, **10**, 2542–2543.
- Halothore, R. N., S. E. Schwartz, J. I. Michalsky, G. P. Anderson, R. A. Ferrare, B. N. Holben, and H. M. Ten Brink (1997), Comparison of model estimated and measured direct-normal solar irradiance, *J. Geophys. Res.*, **102**, 29,991–30,002.
- Haywood, J. M., V. Ramaswamy, and B. J. Soden (1999), Tropospheric aerosol climate forcing in clear-sky satellite observations over the oceans, *Science*, **283**, 1299–1303.
- Haywood, J. M., P. N. Francis, M. D. Glew, and J. P. Taylor (2001a), Optical properties and direct radiative effect of Saharan dust: A case study of two Saharan dust outbreaks using aircraft data, *J. Geophys. Res.*, **106**, 18,417–18,430.
- Haywood, J. M., P. N. Francis, I. Geogdzhayev, M. Mishchenko, and R. Frey (2001b), Comparison of Saharan dust aerosol optical depths retrieved using aircraft mounted pyranometers and 2-channel AVHRR algorithms, *Geophys. Res. Lett.*, **28**, 2393–2396.
- Haywood, J., P. Francis, S. Osborne, M. Glew, N. Loebe, E. Highwood, D. Tanré, G. Myhre, P. Formenti, and E. Hirst (2003), Radiative properties and direct radiative effect of Saharan dust measured by the C-130 aircraft during SHADE: 1. Solar spectrum, *J. Geophys. Res.*, **108**(D18), 8577, doi:10.1029/2002JD002687.
- Holben, B. N., et al. (1998), AERONET: A federated instrument network and data archive for aerosol characterization, *Remote Sens. Environ.*, **66**, 1–16.
- Huebert, B. J., T. Bates, P. B. Russell, G. Shi, Y. J. Kim, K. Kawamura, G. Carmichael, and T. Nakajima (2003), An overview of ACE-Asia: Strategies for quantifying the relationships between Asian aerosols and their climatic impacts, *J. Geophys. Res.*, **108**(D23), 8633, doi:10.1029/2003JD003550.
- Jacobson, M. Z. (2001), Global direct radiative forcing due to multicomponent anthropogenic and natural aerosols, *J. Geophys. Res.*, **106**, 1551–1568.
- Jones, A., and A. Slingo (1996), Predicting cloud-droplet effective radius and indirect sulphate aerosol forcing using a general circulation model, *Q. J. R. Meteorol. Soc.*, **122**, 1573–1595.
- Kalashnikova, O. V., and I. N. Sokolik (2002), Importance of shapes and compositions of wind-blown dust particles for remote sensing at solar wavelengths, *Geophys. Res. Lett.*, **29**(10), 1398, doi:10.1029/2002GL014947.
- Kinne, S., T. P. Ackerman, M. Shiobara, A. Uchiyama, A. J. Heymsfield, L. Milosevich, J. Wendell, E. W. Eloranta, C. Purgold, and R. W. Bergstrom (1997), Cirrus cloud radiative and microphysical properties from ground observations and in situ measurements during FIRE 1991 and their application to exhibit problems in cirrus solar radiative transfer modeling, *J. Atmos. Sci.*, **54**, 2320–2344.
- Krueger, B. J., V. H. Grassian, A. Laskin, and J. P. Cowin (2003), The transformation of solid atmospheric particles into liquid droplets through heterogeneous chemistry: Laboratory insights into the processing of calcium containing mineral dust aerosol in the troposphere, *Geophys. Res. Lett.*, **30**(3), 1148, doi:10.1029/2002GL016563.
- Levy, R. C., L. Remer, D. Tanré, Y. Kaufman, C. Ichoku, B. Holben, J. Livingston, P. Russell, and H. Maring (2003), Evaluation of the MODIS retrievals of dust aerosol over the ocean during PRIDE, *J. Geophys. Res.*, **108**(D19), 8594, doi:10.1029/2002JD002460.
- Li-Jones, X., and J. M. Prospero (1998), Variations in the size distribution of non-sea-salt sulphate aerosol in the marine boundary layer at Barbados: Impact of African dust, *J. Geophys. Res.*, **103**, 16,073–16,084.
- Livingston, J. M., et al. (2003), Airborne sunphotometer measurements of aerosol optical depth and columnar water vapor during the Puerto Rico Dust Experiment, and comparison with land, aircraft, and satellite measurements, *J. Geophys. Res.*, **108**(D19), 8588, doi:10.1029/2002JD002520.
- Mishchenko, M. I., L. D. Travis, R. A. Kahn, and R. A. West (1997), Modeling phase functions for dustlike tropospheric aerosols using a shape mixture of randomly oriented polydisperse spheroids, *J. Geophys. Res.*, **102**, 16,831–16,847.
- Moulin, C., H. R. Gordon, V. F. Banzon, and R. H. Evans (2001), Assessment of Saharan dust absorption in the visible from SeaWiFS imagery, *J. Geophys. Res.*, **106**, 18,239–18,249.
- O'Dowd, C. D., J. A. Lowe, and M. H. Smith (1999), Coupling sea-salt and sulphate interactions and its impact on cloud droplet concentration predictions, *Geophys. Res. Lett.*, **26**, 1311–1314.
- Prospero, J. M., P. Ginoux, O. Torres, S. E. Nicholson, and T. E. Gill (2002), Environmental characterization of global sources of atmospheric soil dust identified with the Nimbus 7 Total Ozone Mapping Spectrometer (TOMS) absorbing aerosol product, *Rev. Geophys.*, **40**(1), 1002, doi:10.1029/2000RG000095.
- Raes, F., T. Bates, F. Mcgovern, and M. van Liedekerke (2000), The 2nd Aerosol Characterization Experiment (ACE-2): General overview and main results, *Tellus, Ser. B*, **52**(2), 111–125.
- Reagan, J. A., Q. Gao, B. M. Herman, T. Caudill, and D. Flittner (1992), Aureole corrections to optical depths determined by solar photometry under turbid volcanic conditions, paper presented at Chapman Conference on Climate, Volcanism, and Global Change, Hilo, Hawaii, AGU, Washington, D.C., 23–27 March.
- Redemann, J., S. Masonis, B. Schmid, T. Anderson, P. Russell, J. Livingston, O. Dubovik, and A. Clarke (2003), Clear-column closure studies of aerosols and water vapor aboard the NCAR C-130 in ACE-Asia, 2001, *J. Geophys. Res.*, **108**(D23), 8655, doi:10.1029/2003JD003442.



- Reid, J. S., et al. (2003), Analysis of measurements of Saharan dust by airborne and ground-based remote sensing methods during the Puerto Rico Dust Experiment (PRIDE), *J. Geophys. Res.*, *108*(D19), 8586, doi:10.1029/2002JD002493.
- Remer, L., and Y. Kaufman (1998), Dynamic aerosol model: Urban/industrial aerosol, *J. Geophys. Res.*, *103*, 13,859–13,871.
- Rosenfeld, D. (2000), Suppression of rain and snow by urban and industrial air pollution, *Science*, *287*, 1793–1796.
- Rosenfeld, D., R. Lahav, A. P. Khain, and M. Pinsky (2002), The role of sea-spray in cleansing air pollution over ocean via cloud processes, *Science*, *297*, 1667–1670.
- Russell, P. B., and J. Heintzenberg (2000), An overview of the ACE 2 Clear Sky Column Closure Experiment (CLEARCOLUMN), *Tellus, Ser. B*, *52*, 463–483.
- Russell, P. B., et al. (1993a), Pinatubo and pre-Pinatubo optical-depth spectra: Mauna Loa measurements, comparisons, inferred particle size distributions, radiative effects, and relationship to lidar data, *J. Geophys. Res.*, *98*, 22,969–22,985.
- Russell, P. B., et al. (1993b), Post-Pinatubo optical depth spectra vs. latitude and vortex structure: Airborne tracking sunphotometer measurements in AASE II, *Geophys. Res. Lett.*, *20*, 2571–2574.
- Schmid, B., et al. (2003), Column closure studies of lower tropospheric aerosol and water vapor during ACE-Asia using airborne Sun photometer, airborne in situ and ship-based lidar measurements, *J. Geophys. Res.*, *108*(D23), 8656, doi:10.1029/2002JD003361.
- Shettle, E. P., and R. W. Fenn (1979), Models of aerosols of lower troposphere and the effect of humidity variations on their optical properties, *U.S. Air Force Cambridge Res. Lab. Tech. Rep., AFCRL-TR 79 0214*, 100 pp.
- Shiobara, M., and S. Asano (1994), Estimation of cirrus optical thickness from Sun photometer measurements, *J. Appl. Meteorol.*, *33*, 672–681.
- Sinyuk, S., O. Torres, and O. Dubovik (2003), Combined use of satellite and surface observations to infer the imaginary part of refractive index of Saharan dust, *Geophys. Res. Lett.*, *30*(2), 1081, doi:10.1029/2002GL016189.
- Smirnov, A., B. N. Holben, Y. J. Kaufman, O. Dubovik, T. F. Eck, I. Slutsker, C. Pietras, and R. N. Halthore (2002), Optical properties of atmospheric aerosol in maritime environments, *J. Atmos. Sci.*, *59*, 501–523.
- Sokolik, I. N., and O. B. Toon (1996), Direct radiative forcing by anthropogenic mineral aerosols, *Nature*, *381*, 681–683.
- Tanré, D., Y. J. Kaufman, B. N. Holben, B. Chatenet, A. Karnieli, F. Lavenue, L. Blarel, O. Dubovik, L. A. Remer, and A. Smirnov (2001), Climatology of dust aerosol size distribution and optical properties derived from remotely sensed data in the solar spectrum, *J. Geophys. Res.*, *106*, 18,205–18,217.
- Tegen, I., A. A. Lacis, and I. Fung (1996), The influence on climate forcing of mineral aerosols from disturbed soils, *Nature*, *380*, 419–422.
- Wang, J., et al. (2002), Clear-column radiative closure during ACE-Asia: Comparison of multiwavelength extinction derived from particle size and composition with results from sunphotometry, *J. Geophys. Res.*, *107*(D23), 4688, doi:10.1029/2002JD002465.
- Whitby, K. T. (1978), The physical characteristics of sulfur aerosols, *Atmos. Environ.*, *12*, 135–159.
- Wiscombe, W. J., and G. W. Grams (1976), The backscattered fraction in two-stream approximations, *J. Atmos. Sci.*, *33*, 2440–2451.

M. Box, School of Physics, University of New South Wales, Sydney, New South Wales 2052, Australia. (m.box@unsw.edu.au)

O. Dubovik, Goddard Earth Sciences and Technology Center, NASA Goddard Space Flight Center, Code 912, Greenbelt, MD 20771, USA. (dubovik@aeronet.gsfc.nasa.gov)

B. N. Holben, Laboratory for Atmospheres, NASA Goddard Space Flight Center, Code 912, Greenbelt, MD 20771, USA. (brent@aeronet.gsfc.nasa.gov)

J. M. Livingston, SRI International, 333 Ravenswood Avenue, Menlo Park, CA 94025, USA. (jlivingston@mail.arc.nasa.gov)

S. A. Ramirez, J. Redemann, and B. Schmid, Bay Area Environmental Research Institute, 560 3rd Street West, Sonoma, CA 95476, USA. (s.a.ramirez@mail.arc.nasa.gov; jredemann@mail.arc.nasa.gov; bschmid@mail.arc.nasa.gov)

P. B. Russell, NASA Ames Research Center, MS 245-5, Moffett Field, CA 94035-1000, USA. (philip.b.russell@nasa.gov)

J. Wang, Brookhaven National Laboratory, Upton, NY 11973, USA. (jian@bnl.gov)